HHS Public Access

Author manuscript

Bone. Author manuscript; available in PMC 2019 May 01.

Published in final edited form as:

Bone. 2019 March ; 120: 285–296. doi:10.1016/j.bone.2018.11.003.

Deletion of nicotinic acetylcholine receptor alpha9 in mice resulted in altered bone structure

Lisa Baumann[a], **Vivien Kauschke**[a], **Anna Vikman**[b], **Lutz Dürselen**[b], **Gabriela Krasteva-Christ**[c], **Marian Kampschulte**[d], **Christian Heiss**[e], **Kathleen T. Yee**[f], **Douglas E. Vetter**[f], **Katrin Susanne Lips**[a,*]

[a]Experimental Trauma Surgery, Justus-Liebig-University Giessen, Aulweg 128, 35392 Giessen, Germany

[b]Institute of Orthopaedic Research and Biomechanics, Center for Trauma Research, Ulm University Medical Centre, Helmholtzstrasse 14, 89081 Ulm, Germany

[c]Institute of Anatomy and Cell Biology, Saarland University, Kirrberger Straße, 66421 Homburg, Germany

[d]Laboratory of Experimental Radiology, Justus-Liebig-University Giessen, Schubertstrasse 81, 35392 Giessen, Germany

[e]Department of Trauma, Hand, and Reconstructive Surgery Giessen, University Hospital of Giessen-Marburg, Rudolf-Buchheim-Str. 7, 35392 Giessen, Germany

[f]Department of Neurobiology and Anatomical Sciences, University Mississippi Medical Center, Jackson, MS, USA

Abstract

Alterations in bone strength and structure were found in knockout (KO) mouse strains with deletion of several acetylcholine receptors. Interestingly, the expression of the nicotinic acetylcholine receptors (nAChR) subunit α10 was down-regulated in osteogenic differentiated mesenchymal stem cells of patients with osteoporosis whereas the expression of subunit α9 was not altered. Since nAChR subunits α9 and α10 are often combined in a functional receptor, we analyzed here the bone of adult female KO mice with single deletion of either nAChR alpha9 (α9KO) or alpha10 (α10KO).

Biomechanical testing showed a significant decrease of bending stiffness and maximal breaking force in α9KO compared to their corresponding wild type mice. Furthermore, an increase in trabecular pattern factor (Tb.Pf) and structure model index (SMI) was detected by μCT in α9KO indicating reduced bone mass. On the mRNA level a decrease of Collagen Iα1 and Connexin-43 was measured by real-time RT-PCR in α9KO while no alteration of osteoclast markers was

*Corresponding author at: Experimental Trauma Surgery, Justus-Liebig-University Giessen, Aulweg 128, 35392 Giessen, Germany. Katrin.S.Lips@chiru.med.uni-giessen.de (K.S. Lips).

Disclosures

All authors state that they have no conflict of interest.

Supplementary data to this article can be found online at https://doi.org/10.1016/j.bone.2018.11.003.

detected in either mouse strain. Using electron microcopy we observed an increase in the number of osteocytes that showed signs of degeneration and cell death in the α9KO compared to their wild type mice, while α10KO showed no differences.

In conclusion, we demonstrate alterations in bone strength, structure and bio-marker expression in α9KO mice which imply the induction of osteocyte degeneration. Thus, our data suggest that nAChR containing the α9 subunit might be involved in the homeostasis of osteocytes and therefore in bone mass regulation.

Keywords

Bending stiffness; Micro-CT; Connexin-43; Collagen 1α1; nAChR α10; Non-neuronal cholinergic system

1. Introduction

Alterations in bone strength and structure were found in knockout (KO) mice with deletion of several acetylcholine receptors [1–3]. Nicotinic acetylcholine receptors (nAChR) are pentameric ion channels built by a combination of alpha (α1-α10) and beta (β1-β4) subunits or solely by alpha subunits in the case of homopentamers (α7, α9) or as alpha-heteropentamer (α9α10) [4]. Electrophysiological analysis of combined α9 and α10 subunits demonstrated 100-fold more functional receptors compared to α9 homopentamers [5,6]. nAChR α9α10 are activated by acetylcholine, but not by nicotine. In addition, they are sensitive to muscarine and atropine and show therefore mixed ionotropic and metabotropic profile [6]. The α9α10 nAChR was first identified in the outer hair cells of cochlea where it is involved in auditory signaling [5]. Additionally, the α9α10 nAChR are associated with chronic pain signaling and therefore seem to be a promising target for analgesic medications [7]. Moreover α9α10 nAChR were found in immune cells (B-cells, T-cells) where they lack single cell responses to acetylcholine (ACh) typically expected for ionotropic receptors [8,9]. The α9α10 nAChR provokes long-term intracellular cascades by interacting with calcium stores in response to inflammatory triggers [8,9]. Receptors containing one or both α9 and α10 subunits were found in several neuronal and non-neuronal tissues e.g. brain regions [10], breast tumors [11,12], keratinocytes [13], and bronchial epithelial cells [14]. In these systems an involvement in inner (mitochondrial-derived) apoptotic pathways [10], stimulation of proliferation [11,14], and a cell-type specific transformation into cancerogenic cells [12] is indicated. The role of α9 nAChR in skin keratinocytes has been analyzed in more detail. nAChR α9 control cell shape, cytoplasm mobility, wound re-epithelialization, proper migration as well as cell-cell and cell-matrix contacts via phosphorylation of specific adhesion molecules [13].

nAChR subunit α9 mRNA was found to be highly expressed in chondrocytes and/or osteoblasts of the developing labyrinthine bone as well as in bone marrow cells of juvenile and adult rats as determined by in-situ hybridization [15]. Expression of nAChR subunits α9 and/or α10 was also described in hematopoietic stem cells and several phases of differentiating blood cells, including leucocytes, monocytes, and bone marrow macrophages [1,2,8]. In addition, bone marrow contains amongst others endothelial and smooth muscle

cells, nerve fibers, adipocytes, and mesenchymal stem cells (MSC) that are precursors of osteoblasts, chondrocytes, and adipocytes. Zablotni et al. reported the expression of α9 and α10 subunits in female native MSC and in osteogenic differentiated MSC of both genders [16]. An up-regulation of α10 mRNA level was detected in osteoblasts of healthy compared to osteoporotic donors [16]. Both α9 and α10 nAChR mRNA were found in native and osteogenic differentiated murine osteoblast from the cell line MC3T3, in osteoblastic human osteosarcoma cell line SAOS-2 [17], in rat maxilla [18,19] whereas in osteocytes only the α10 subunit and in murine tibia the α9 subunit were detected [20].

To further investigate the functional role of the nAChR subunits α9 and α10 in bone, we analyzed mice carrying a global constitutive knockout (KO) of the single subunits. Recently it was shown that deletion of mAChR M3 and nAChR α2 in mice resulted in bone alterations similar to osteoporosis [2,3]. Here, we used biomechanical, radiological, histological, cell and molecular biological methods as well as transmission electron microscopy to analyze whether either the α9, α10 or both subunits are involved in alterations of bone structure, strength and homeostasis.

2. Materials and methods

2.1. Mice

Female mice with a deletion of nAChR subunit α9 (n = 8, 129S-*Chrna9*$^{tm1Bedv/}$J) or subunit α10 (n = 8, 129S4-*Chma10*$^{tm1Bedv/}$Mmucd) and their corresponding wild type mice (α9 n = 8, α10: n = 8) were euthanized at the age of 16–20 weeks according to the recommendations of the AVMA Guidelines for the Euthanasia of Animals. Afterwards the bones were extracted for subsequent analysis. The breeding pair was a kind gift of Dr. Douglas E. Vetter [21,22]. The mice were bred in the animal facility of the Justus-Liebig-University Giessen with a 12 h day and night cycle and free access to water and food. All animal experiments were performed in accordance with the ARRIVE guidelines and the EU Directive 2010/63/EU and had been declared to the Animal Welfare Officer of the Justus-Liebig-University (Registration No.: M_492 and M_521, Giessen, Germany). A separate set of male and female α9KO (n = 18) and α9WT (n = 6) at an age of 17 to 22 weeks were used for mouse hang test at the UMMC Animal Behavior Core Facility.

2.2. Mouse hang test

A 55 cm long, 2 mm thick metallic wire was secured to two vertical poles. The wire was stretched across the vertical poles approximately 40 cm above a thick layer of standard bedding into which the mouse falls if they release their grip on the wire. The “longest suspension time” method was used, and the test was run as follows. 1. The mouse was handled by the tail and allowed to grasp the middle of the wire with its forelimbs. The mouse was then gently lowered so that its hind paws did not grasp the wire. 2. The tail was then released while the mouse grasped the wire. Upon release, a timer was started. 3. The time until the mouse completely releases its grasp and falls into the bedding was recorded. A fixed maximum time for hanging without falling was 180 s. 4. If the mouse did not reach the maximum time limit, it was given three trials per session, with a 1 min recovery period between trials. The maximum hang time was recorded as the longest single hang. In all

cases, this was the first attempt. If a mouse reached the maximum time limit, the testing was considered complete. Mice underwent only one session with a maximum of three trials.

2.3. Biomechanical analysis of femoral bones

After extraction of left femur it was covered with a 0.9% NaCl moistened pad and stored at − 20 °C. Prior to the measurement, the femur was thawed and the proximal part fixed in an aluminum cylinder 8 mm in diameter using iCEM self-adhesive glue (Heraeus-Kulzer, Hanau, Germany). The aluminum cylinder was fixed in a hinge joint of a material testing machine (Zwick Z10, Ulm, Germany), serving as the proximal support for the bending test whereas the distal end of the femur was rested unfixed on a distal bending support with a distance of 6.5 mm to the force transducer. After two test cycles the bone was broken in the third cycle and the data were collected by testXpertll software (Version 3.2, Zwick). Using the load-deformation curve, the maximal breaking force and bending stiffness were calculated as described previously [23].

2.4. Micro-computed tomography

The right femur and vertebra L1 were fixed in 4% phosphate buffered paraformaldehyde, washed in 0.1 M phosphate buffer (pH 7.3) and scanned with a high-resolution micro-computed tomograph (Micro-CT 1173, SkyScan, Kontich, Belgium) at 5.69 pm voxel size and 16 bit gray scale range as described earlier [24]. To define volume of interest (VOI) of distal metaphysis, the growth plate was used as a reference level. The trabecular area of the femur metaphysis including 309 slices (1.753 mm) was measured with a distance of 0.216 mm from reference level. Cortical distal and mid diaphysis, each 80 slices (0.45 mm), were examined distantly at 2.179 mm and 5.497 mm from reference level. According to the manual “Structural parameters measured by the SkyscanTM CT-analyzer software” and the review of Bouxsein et al., regions of interest (ROIs) were selected with a short distance to endocortical surface [25]. The whole trabecular area of vertebral body was manually scanned excluding primary spongiosa and cartilage. BMD and TMD measurement was performed using calibrating phantoms with defined calcium hydroxyapatite density.

Regarding the cortical regions of femur’s diaphysis, the following parameters [25] were calculated: total cross-sectional area inside the periosteal envelope (Tt.Ar), cortical bone area (Ct.Ar), cortical area fraction (Ct.Ar/Tt.Ar), cortical thickness (Ct.Th), total porosity (Po.tot) and the tissue mineral density (TMD). The following parameters were calculated for the trabecular bone of femur and vertebra L1: bone volume fraction (BV/TV), specific bone surface (BS/BV), trabecular thickness (Tb.Th), trabecular separation (Tb.Sp), trabecular pattern factor (Tb.Pf), structure model index (SMI), and bone mineral density (BMD). 3D-color coded models of trabecular thickness were generated with CTvox (version, 3.3.0r1403 (64bit), SkyScan).

2.5. Histology, enzyme- and immunohistochemistry, and histomorphometry

After extraction, vertebrae L3 were fixed in 4% phosphate buffered paraformaldehyde, washed carefully in 0.1 M phosphate buffer (pH 7.3), decalcified in 10% ethylenediaminetetraacetate (EDTA), and dehydrated with a graded series of ethanol and embedded in paraffin. Dewaxed 5 pm thick sections were used for enzyme histochemical

staining of alkaline phosphatase (ALP) and tartrate resistant acid phosphatase (TRAP) as described previously [24]. For immunohistochemistry dewaxed sections were preincubated in 3% H_2O_2 in Tris-NaCl buffer (TBS) with 0.025% Triton-X for 5 min to block endogenous peroxidase. Primary antibodies against (i) sclerostin (1:100 diluted, abcam, Cambridge, UK) and (ii) Connexin-43 (Cx43) (1:100 diluted, Thermo Fisher Scientific, Waltham, MA, USA) were incubated overnight in dilution buffer (Dako, Glostrup, Denmark) at 4 °C. Thereafter sections were processed with (i) an anti-rabbit secondary antibody that is conjugated with HRP labeled polymer (Dako EnVision) or (ii) a goat anti-rabbit secondary antibody (diluted 1:500, Vector, Burlingame, CA, USA) for 30 min. A 5 min incubation with 3,3′-diaminobenzidine substrate-chromogen (Dako) staining of sclerostin was completed. Immunostaining for Cx43 was accomplished using a 30 min incubation with an avidin and biotin peroxidase system (Vectastain Elite ABC, Vector) and 5 min incubation using a substrate kit for peroxidase (Nova Red, Vector). Nuclei were counterstained with hematoxylin and the sections were coverslipped with Depex (Serva, Heidelberg, Germany).

Vertebrae L1 were also fixed in 4% paraformaldehyde and washed with phosphate buffer, before they were dehydrated with a graded series of ethanol and then embedded in Technovit 9100 (Heraues Kulzer, Hanau, Germany) as described in detail by the manufacturer's protocol. Sections with a thickness of 5 pm were histologically stained with Kossa-van-Gieson method as described earlier [24]. Staining with silver nitrate solution (Sigma-Aldrich, Steinheim, Germany) and Gieson's mixture (Chroma/Waldeck, Münster, Germany) was used to differentiate between mineralized bone matrix and osteoid. Photos were taken with microscope Axiophot-2 (Zeiss, Jena, Germany) fitted with digital camera (Leica DC 500, Leica, Bensheim, Germany) and corresponding software Leica IM1000 (Version 4.0, Leica Microsystems, Cambridge, UK).

The trabecular bone of vertebral body was analyzed histomorphometrically using Adobe Photoshop CS5 (Adobe, San Jose, CA, USA) and traphisto software [26]. We measured the relative perimeter of ALP staining (ALP.Pm/B.Pm), the number of osteoclasts per bone perimeter (N.Oc/B.Pm), the relative osteoclast perimeter (Oc.Pm/B.Pm), the number of sclerostin positive osteocytes per bone area (Scl.Ot/B.Ar), and the relative osteoid area (O.Ar/B.Ar).

2.6. Real-time reverse transcriptase polymerase chain reaction (real-time RT-PCR)

Vertebrae Th10 was transferred into RNA-later (Ambion Applied Biosystems, Foster City, CA, USA) directly after euthanasia. For RNA isolation tissue was homogenized in lysis buffer (Qiazol, Qiagen, Hilden, Germany) with a vibratory mill (MM400, Retsch, Haan, Germany). Then 200 µL of chloroform (Sigma-Aldrich, St.-Louis, MO, USA) were added and the samples were centrifuged for 15 min at 4 °C. RNA was collected from the aqueous phase and mixed with the same amount of 70% ethanol. The solution was transferred into RNeasy Mini Spin Columns (RNeasy Lipid Tissue Mini Kit, Qiagen) and centrifuged to enable the binding of RNA to the column membrane. RNA was washed with several buffers (kit component, RNeasy Lipid Tissue Mini Kit, Qiagen) and eluted with RNase-free water. The RNA concentration and purity were determined using a Nanodrop photometer (ND-1000, Nanodrop Technologies, Wilmington, NC, USA). RNA was stored at − 80 °C

before reverse transcription into cDNA. For elimination of contaminations with genomic DNA 750 ng RNA was incubated with 3 μL wipeout buffer (Qiagen) at 42 °C in a thermo cycler (TC-3000, Techne, Bibby Scientific, USA). Afterwards reverse transcriptase (RT), buffers, RT primer mix (Quantitect Reverse Transkriptase Kit, Qiagen) were added and incubated for 30 min at 42 °C. After inactivation of reverse transcriptase for 3 min at 95 °C, samples were stored at − 20 °C. Real-time RT-PCR was performed using the Quantifast Sybr Green PCR Kit (Qiagen) according to the manufacturer's protocol. In brief, 0.2 μL of primers (Table 1, MWG Biotech, Ebersberg, Germany) with 0.8 μL RNase-free water and 5 μL of Quantifast Mastermix were diluted with 4 μL cDNA or RNase-free water to a volume of 10 μL. The dilution was transferred into capillaries (Roche, Mannheim, Germany), centrifuged 20 s at 2000 rpm and processed in a LightCycler 2.0 (Roche, Basel, Switzerland) with the following protocol: 5 min at 95 °C for denaturation and then 40 cycles of 10 s at 95 °C, 30 s at 60 °C for annealing and elongation. Afterwards the purity of PCR product was analyzed by melting curve analysis. Additionally, the following controls were performed during real-time RT-PCR: a) PCR without template, b) cDNA synthesis without addition of reverse transcriptase to control for contaminations with genomic DNA, c) determination of PCR efficiency and slope, and d) samples were analyzed in doublets. The value of the crossing point (CP) determines the point where the amplification curve crosses the vertical threshold line was normalized to the reference gene β-actin.

2.7. Transmission electron microscopy (TEM)

Samples of L4 vertebrae were immersion-fixed 6 h in a solution of 2% paraformaldehyde and 0.02% picrinic acid in phosphate buffer (pH 7.3), washed with 0.1 M cacodylate buffer and post-fixed for 2 h in 1% osmium tetroxide. Specimens were dehydrated in a graded series of ethanols followed by embedding in Epon (Serva, Heidelberg, Germany) Ultrathin sections were cut and then analyzed by TEM (EM 912, Zeiss, Oberkochen, Germany) equipped with a 2 K slow-scan CCD camera. Pictures were scored by two blinded investigators. Osteocytes of 5 α9KO (n = 255), 5 α9WT (n = 177), 3 α10KO (n = 102), and 3 α10WT (n = 114) mice were evaluated. A score of 1 was given to healthy active osteocytes, 2 to osteocytes showing signs of cell degeneration and 3 to dying osteocytes. Degeneration of osteocytes was defined by the presence of at least two of the following characteristics: (i) extended pericellular space, (ii) folding of the cytoplasmic membrane, (iii) enlarged spaces between the nuclear membranes, and (iv) occurrence of enlarged vesicles.

2.8. Cell culture experiments

Osteoblasts were cultured from neonatal α9KO (n = 10) and α9WT (n = 7) C57BL/6J mice at day 1–4 according to the protocol of [27,28]. The neonatals were a kind gift of Dr. Claudia Dames (Institute of Medical Immunology, Charite - Universitätsmedizin Berlin, Germany). In brief, calvaria and long bones were incubated in 1 mg/mL collagenase (Capricorn Scientific, Ebsdorfergrund, Germany) and 4 mM ethylene diamine tetra acetic acid (EDTA) at 37 °C and centrifuged for 5 min at 1.500 *g* at 4 °C. Isolates were seeded in 24 well plates for 4 d at 37 °C and 5% CO_2 and passaged with 0.005% trypsin (Gibco, Life Technologies, Carlsbad, USA). Cells of passage 2 (13.441 cells/cm^2) were used for osteogenic differentiation in α-minimum essential medium (MEM, Gibco)

containing 10% fetal bovine serum (FBS, PAN Biotech, Aidenbach, Germany), 10^{-7}M dexamethasone (Sigma, St. Louis, MO, USA), 50 pg/mL sodium L-ascorbate (Sigma), 2×10^{-3} M β-*glycero* phosphate hydrate (Sigma), and gentamicin/amphotericin (Gibco) for 7 d. Then, mineralization was determined using the Senso- Lyte pNPP alkaline phosphatase assay (AnaSpec, Fermont, CA, USA) and collagen deposition was analyzed by a Picro-Sirius-Red assay (Abcam, Cambridge, UK). Subsequent histomorphometry calculated the area of positive collagen type 1 and 3 staining.

2.9. Statistical analysis

Statistical analyses were performed with SPSS software (version 23, SPSS Institute Inc., Chicago, USA). After testing for normal distribution by Kolmogorov-Smirnov test we used a t-test, Wilcoxon Rank Sum Test, or Kruskal-Wallis test followed by non-parametric Mann-Whitney test. Significance level was set at p value of < 0.05. Results were reported as mean ± standard deviation and graphs were generated with Prism (version 6.02, GraphPad Software Inc., La Jolla, USA). nAChR α9 and α10 animals were not compared due to the genetic manipulation being on different mouse strains.

3. Results

3.1. Mouse hang test

To determine mouse muscle force and physical activity in vivo we performed the hang test which did not result in significant differences between α9KO and α9WT ($p < 0.119$; Fig. 1).

3.2. Bone strength

The body weight of α9KO (25.16 ± 1.7 g) was significantly reduced compared to α9WT (27.86 ± 2.26 g, $p < 0.05$, Fig. 2A). The mid-diaphysial region of left femur was tested by a biomechanical three-point-bending test. The bending stiffness of α9KO (2597.17 ± 169.08 Nmm^2, Fig. 2B) as well as the maximal breaking force (9.33 ± 0.41 N) were significantly decreased compared to α9WT (2944.63 ± 96.27 Nmm^2 and 10.65 ± 0.61 N, each $p < 0.001$, Fig. 2C). No significant changes in body weight, bending stiffness and maximal breaking force were measured for α10KO compared to the control α10WT (Fig. 2).

3.3. Microarchitecture of cortical bone

The microstructure of cortical bone of mid (Fig. 3) and distal diaphysis (Fig. S1) of right femur was analyzed by pCT. The Ct.Ar (Fig. 3A) as well as Tt.Ar (Fig. 3B) were significantly reduced in α9KO (Ct.Ar 0.90 ± 0.05 mm^2; Tt.Ar 2.02 ± 0.09 mm^2) compared to α9WT (Ct.Ar 1.01 ± 0.04 mm^2, $p < 0.05$; Tt.Ar 2.26 ± 0.17 mm^2, $p < 0.01$) while Ct.Ar/Tt.Ar showed no significant differences in the mid diaphysis (Fig. 3C). No changes were observed for the α10KO and WT. Similar results were measured in the distal diaphysis of right femur (Fig. S1A–C). In addition, we measured significantly decreased total porosity (Po.tot) in α9KO (0.06 ± 0.08%) compared to α9WT (0.18 ± 0.13%, $p < 0.05$). Ablation of the α10 subunit did not produce changes in Po.tot (Fig. 3D) in mid diaphysis. In distal diaphysis neither α9 nor α10KO showed any significant alterations (Fig. S1D). Also the Ct.Th was not changed in α9 and α10KO for both cortical regions (Figs. 3E and S1E) which was verified by μCT images (Fig. 3G–H). TMD was significantly decreased in α9KO

of both regions (mid diaphysis 1.33 ± 0.01 g/cm^3, distal diaphysis 1.20 ± 0.01 g/ cm^3) compared to α9WT (mid diaphysis 1.37 ± 0.02 g/cm^3, distal diaphysis 1.23 ± 0.02 g/cm^3, each $p < 0.01$, Figs. 3F and S1F) while α10KO was not affected.

3.4. Microarchitecture of trabecular bone

The microstructure of the trabecular bone of right femur and vertebra L1 was scanned with μCT and typical parameters for cancellous bone were calculated (Fig. 4). The relative bone volume (BV/TV) of femur showed no significant alterations for α9 and α10KO compared to their WT controls (Fig. 4A). The Tb.Th was significantly declined in α9KO (41 ± 2 μm) compared to α9WT (44 ± 1 μm, $p < 0.01$) whereas no affect in α10KO was observed (Fig. 4B). Regarding Tb.Sp no changes were found for α9KO and WT while we measured an increase for α10KO (0.24 ± 0.014 mm) compared to α10WT (0.22 ± 0.018 mm, $p < 0.01$, Fig. 4C). The relative bone surface (BS/ BV, 96.60 ± 3.19 mm^{-1}), Tb.PF (31.03 ± 2.39 mm^{-1}) as well as the SMI (2.12 ± 0.07) was significantly increased in α9KO compared to α9WT (BS/BV 91.41 ± 1.86 mm^{-1}, $p < 0.01$; Tb.PF 27.13 ± 1.24 mm^{-1}, $p < 0.05$; SMI 2.02 ± 0.05, $p < 0.05$; Fig. 4D–F). In accordance with these results, values of Tb.Pf (7.21 ± 1.66 mm^{-1}) and SMI (1.06 ± 0.09) were increased in vertebrae of α9KO compared to α9WT (Tb.Pf 3.96 ± 1.90mm^{-1}, SMI 0.79 ± 0.14, each $p < 0.05$, Fig. 4E–F). Regarding α10 mice, no significant alterations were determined for BS/BV (Fig. 4D) and Tb.Pf (Fig. 4E) of femur as well as vertebrae (Fig. 4G–H). The SMI was significantly increased for α10KO (1.69 ± 0.09) compared to α10WT (1.58 ± 0.12, $p < 0.001$, Fig. 4F) in femur whereas SMI of vertebrae showed no significant differences (Fig. 4H). In addition, we found no significant changes in BV/TV, Tb.Th, Tb.Sp, BS/BV and BMD of vertebrae as well as of BMD of femur (Fig. S2E, F). To visualize the alteration in trabecular microstructure, a 3D model was generated (Fig. 4I–J) where trabecular size was color coded (blue: app. 10–20 μm, green: app. 30–50 μm, red: app. 60–100 μm).

3.5. Osteoblasts

Changes in osteoblast activity were either evaluated by real-time RT-PCR of typical osteoblast markers or using histological and subsequent histomorphometrical methods. ALP, one of the most prominent enzymes of osteoblast hydroxyapatite synthesis, was stained by enzyme histochemistry with a deep violet labeling of osteoblasts mostly situated at the trabecular surface. In addition, the violet ALP staining was also found in secreted vesicles of osteoblasts localized in osteoid and woven bone. Interestingly, in α9KO and α9WT (not shown) only a low amount of ALP positive staining product was found (Fig. 5A) whereas in α10KO and WT a high number of ALP positive structures were observed (Fig. 5B). Here we identified single osteoblast covering the trabecular bone (arrow in Fig. 5B). Subsequent histomorphometrical calculation of the ALP.Pm/B.Pm did not show significant changes in α9 and α10KO compared to their corresponding WT mice (Fig. 5C). In accordance with ALP histology (Fig. 5A–B) ALP.Pm/B.Pm was low in α9KO (8.81 ± 4.27%) and WT (17.84 ± 11.62%) and much higher in α10KO (90.33 ± 7.39%) and α10WT (79.31 ± 21.77%, Fig. 5C). At the mRNA level, ALP was significantly decreased in α10KO (−6.16 ± −0.59 -ΔCP) compared to α10WT(−5.57 ± −0.36-ΔCP, $p < 0.05$) but no regulation was found for α9KO (−6.41 ± −0.54 -ΔCP) and WT (−6.02 ± −0.47 -ΔCP, Fig. 5D). As a second marker, measurement of mRNA expression levels of Col1α1 revealed a significant decrease

in α9KO(−1.38 ± −0.68-ΔCP) compared to α9WT (−0.68 ± −0.35-ΔCP, $p < 0.05$) whereas no significant differences were found for α10 (Fig. 5E). Since Col1α1 holds the highest proportion of organic substances of bone matrix we decided to perform an additional von Kossa-van-Gieson staining to determine the relative osteoid area (O.Ar/B.Ar) by means of histomorphometry. The corresponding results showed neither a regulation of α9 nor of α10KO compared to their WT (Fig. 5F).

In addition to these results regarding osteoblasts in adult murine bone, we evaluated osteoblasts in vitro that were harvested from neonatal α9KO and α9WT mice to answer the question whether the α9KO osteoblasts are fully functional. Bone mineralization was investigated by ALP activity in relation to total protein. No significant changes were measured for α9KO (923 ± 3O7 IU/g) compared to α9WT (793 ± 2l3IU/g, $p = 0.35$l, Fig. 6 A) in osteogenic differentiation medium. As sign of successful osteogenic differentiation we measured a significant increase in ALP activity of α9KO cells in osteogenic medium compared to standard cell culture medium (57O ± 249 IU/g, $p < 0.001$). In accordance, matrix deposition of collagen type 1 and 3 analyzed by Picro-Sirius-Red staining followed by histomorphometry was not significantly modified in α9KO (collagen type 1: 14.51 ± 3.77%, collagen type 3: 3.66 ± 1.26%) compared to α9WT (collagen type 1: 13.15 ± 3.87%, $p = 0.48$, collagen type 3: 4.41 ± 1.89%, $p = 0.34$; Fig. 6B) in osteogenic differentiation medium. In standard cell culture medium the osteoblast did not deposit any collagen type 1 and 3.

3.6. Osteocytes and cell-contacts

Osteocytes are linked with each other by gap junctions that can be identified by its characteristic protein Cx43. By means of real-time RT-PCR we measured a significant decrease in Cx43 expression in α9KO (KO: −7.07 ± −0.62-ΔCP, WT: −6.38 ± −0.49-ΔCP, $p < 0.028$) whereas subunit α10KO (KO:−6.71 ± −0.65-ΔCP, WT: − 6.32 ± − 0.25-ΔCP) showed no regulation at the mRNA level (Fig. 7A). Using a polyclonal antibody against Cx43 we found a distinct macular and fibrillary staining around the osteocytes in trabecular and cortical bone (Fig. 7D). We supposed that this labeling identifies the osteocytic processes and gap junctions between the dendrites. In addition, the cytoplasm of some of the osteocytes, osteoblasts, osteoclasts, and hematopoetic precursors (e.g. megakaryocytes) were also labeled with a moderate intensity by Cx43 antibody as well as some vessels and capillaries.

Since the most typical marker for osteocytes is sclerostin, we also analyzed the mRNA expression of SOST, the sclerostin gene. No expression level change of SOST was detected (α9KO: −7.48 ± −0.32 -ΔCP, WT: −7.73 ± −0.33 -ΔCP; α10KO: −7.57 ± −0.53 -ΔCP, WT:−7.25 ± −0.41-ΔCP, Fig. 7B). Immunohistochemically only some of the osteocytes were labeled while others remained blank. Often the positive labeled osteocytes were localized in the direct neighborhood of negative osteocytes (Fig. 7E). Quantification of the number of sclerostin positive osteocytes per bone area (Scl.Ot/B.Ar) did not reveal significant changes (Fig. 7C). Using TEM we investigated the ultrastructure of osteocytes and determined a highly significant increase in degenerating and dying osteocytes of α9KO compared to α9WT ($p < 0.001$, Fig. 8). For quantification we used a score comprising three subdivisions.

In α9KO, 18.43% cells of osteocytes were scored as 1, 56.47% were scored 2, and 25.1% were scored 3. In the α9WT group 41.24% cells scored 1, 47.46% scored 2, 11.3% scored 3 (Fig. 8D). No changes where observed for α10KO compared to α10WT (α10KO score 1: 28.43%, score 2: 51.96%, score 3: 19.61%, α10WT score 1: 18.42%, score 2: 63.16%, score 3: 18.42%, Fig. 8D).

3.7. Osteoclasts

Osteoclasts were stained by TRAP and analyzed histomorphometrically. No significant changes were detected for N.Oc/B.Pm (α9KO: 5.81 ± 2.07 mm^{-1} WT: 4.52 ± 2.58 mm^{-1}, α10KO: 5.42 ± 2.52 mm^{-1} WT: 7.53 ± 2.21mm^{-1}, Fig. 9A) as well as for Oc.Pm/B.Pm (α9KO: 10.43 ± 4.54 WT: 9.23 ± 7.25, α10KO: 8.25 ± 5.89 WT: 15.29 ± 6.85, Fig. 9B). We investigated the mRNA expression of Cathepsin K (CtsK), the typical degrading enzyme of osteoclasts. No significant changes were measured for CtsK expression in α9KO or α10KO mice (α9KO: −2.50 ± −0.60 -ΔCP, WT: −2.46 ± −0.37 -ΔCP; α10KO: −2.15 ± −0.48 -ΔCP, WT: −1.93 ± −0.38-ΔCP, Fig. 9C).

4. Discussion

In the present study we analyzed the bone tissue of α9 and α10 nAChR subunit KO mouse strains, and compared them to their individual WT mouse strain. The advantage of using KO mice with deletion of single genes is the detailed picture that can be generated about the impact of a single protein in strength and structure of bone as well as presence of bone cells and regulation of typical bone markers. Biomechanical measurements showed a decrease in bending stiffness and maximal breaking force of α9KO compared to their corresponding wild type mice. In contrast, KO of the α10 subunit showed no significant alterations. Bending stiffness and maximal breaking force were measured by a three-point bending test. Reduced strength is often combined with reduced mineralization and therefore commonly found in osteopenic and osteoporotic bone. μCT analysis of cortical bone showed significantly reduced TMD in both diaphysial regions of the left femur in α9KO mice compared to their corresponding wild type. Tt.Ar and Ct.Ar of mid-diaphysial and distal region (Fig. S1) were significantly decreased in the α9KO setting. Noteworthy, the ratio of Ct.Ar/Tt.Ar was not altered. With a view to unchanged Ct.Ar/Tt.Ar ratio and reduced body weight of α9KO, one may speculate that impaired biomechanical properties are caused by smaller long bones. However, decreased mineralization and altered porosity imply alterations in α9KO bone strength caused by abnormal structure and modified bone matrix.

On the microstructural level of cortical bone a significant reduction of porosity was measured in α9KO compared to α9WT. Three hierarchical levels of porosity occur in cortical bone: (i) Collagen-hydroxyapatite porosity that denotes the very small space (in humans: order of 0.01 μm in radius) between the collagen fibers and hydroxyapatite crystals which is usually filled with bound fluids. (ii) Lacunar-canalicular porosity that comprises the pericellular space of osteocytes and their processes which in humans is on the order of 0.1 μm in radii [29]. Neither the collagen-hydroxyapatite and the lacunar-canalicular porosity were analyzed using μCT because of the small size of the pores and limitation of the resolution of our μCT analyses at isotropic voxel size of 5.69 μm. We investigated (iii)

vascular porosity in cortical mid and distal diaphysis. The vascular porosity is defined by the system of Haversian and Volkmann canals in human bone including vessels, nerve fibers, and several cell types (e.g. osteoblasts, macrophages, osteoclasts). Mice cortical bone does not form osteons with Haversian canals [30]. Here, vessels are often found in erosion tunnels and lacunae. The vascular network in rodents is built in series whereas it is organized in parallel in humans [29]. Depending on the mouse strain the vascular porosity reaches values of 0.8 ± 0.2 to 4.8 ± 1.5% [31] which is in accordance to our results of α9WT and α10 mice. It is noteworthy that the vascular porosity of α9KO was significantly reduced (average of 0.06 ± 0.08%). The nAChR subunit α10 is expressed by many locations within the vascular systems whereas subunit α9 shows a distinct expression pattern with occurrence in vascular smooth muscle and endothelial cells in rat and human placenta [32] but absence in e.g. truncus pulmonalis, aorta thoracica [33]. To our knowledge it is not known whether the bone vascular system express nAChR subunits α9 and 10. However, application of nicotine leads to dilation in the most vascular systems [34] whereas in bone it enhances vascular constriction [35]. Since the pharmacological profile of α9α10 does not resemble the typical nAChR [36], not only the presence of these subunits but also their functional role remains unknown in the bone vascular system. In addition to vascular walls, the vascular pores also contain nerve fibers, mesenchymal stem cells, osteoblast precursors and osteoblasts. Regarding nerve fibers, knowledge about α9α10 nAChR is still limited even though the presence of both subunits in several brain regions was recently published [10].

Besides analyzing bone cortex, μCT was used for investigations of the trabecular bone of femur and vertebrae. α9KO mice demonstrated an increase in Tb.Pf, SMI and BS/BV while Tb.Th was reduced. The decline in Tb.Th is one of the typical characteristics of osteopenic and osteoporotic bone. In osteopenia and osteoporosis reduced Tb.Th is usually combined with a decrease in BV/TV and Tb.N and increase in Tb.Sp which we did not detect in α9KO compared to α9WT. Thus, we suggest that α9KO mice do not develop an osteoporotic bone phenotype. This hypothesis is confirmed by the missing regulation of BMD (Fig. S2). However, small perforations and intratrabecular connectivity cannot be calculated by these values but by the Tb.Pf [37]. Well connected trabeculae possess a low Tb.Pf in contrast to more convex formed trabeculae characterized by a greater Tb.Pf. In 3D networks, a high Tb.Pf displays a less connected pattern as determined in spongy bone of postmenopausal females [37]. Thus, α9KO mice showed initial signs of an early stage of bone loss. The dimension free SMI was also significantly increased in α9KO compared to α9WT. An SMI value of 0 describes an ideal plate-like structure of the 3D network of trabeculae and a value of 3 an ideal rod-like structure [38]. In the case of α9KO the trabeculae were arranged in a more rod-like structure than in α9WT. In a murine model of senile osteoporosis, an increase in SMI was measured compared to healthy control mice [39]. Therefore, SMI confirms Tb.Pf results indicating the start of functional bone loss in α9KOs. However, the SMI is critically discussed as a value that can be artificially depressed [40].

Reduced bone mass is often caused by increased enzymatic activity and/or number of osteoclasts. Here, we analyzed osteoclasts by TRAP staining and subsequent histomorphometrical calculation and real-time RT-PCR for CtsK, one of the osteoclastic enzymes which is responsible for degradation of the organic bone matrix. None of the investigated parameters showed any alterations in α9 and α10KO mice compared to their

corresponding wild type controls. Since osteoclasts and osteoblast are two sides of one coin we decided to next analyze bone forming osteoblasts of neonatal α9KO, α9WT and in adult α9 and α10 mice. Neonatal α9KO osteoblasts in vitro were not significantly altered compared to α9WT in osteogenic differentiation as well as standard cell culture medium by means of ALP assay and Picro-Sirius-Red staining. Thus, α9KO osteoblasts seemed to be fully functional. To examine adult osteoblasts we used total bones instead of isolated cells. Regarding hydroxyapaptite synthesis and mineralization, we analyzed ALP by means of histology, histomorphometry, real-time RT-PCR, and Kossa- van-Gieson stained histological sections followed by calculation of the relative osteoid area (O.Ar/B.Ar). None of these parameters were changed in α9KO except for significantly reduced mRNA expression of collagen (Col1α1) of α9KOs compared to α9WTs. Subcutaneous application of nicotine provokes less compact arranged collagen bundles in skin of male adult guinea pigs with enlarged space between the bundles which increases in correlation to enhanced nicotine concentrations [41]. In addition, nicotine administration leads to an increase in collagen type 1 mRNA expression in skin [42] as well as in lung [43] where the stimulatory effect was inhibited in nAChR subunit alpha 7 (α7KO) knockout mice [44]. In bone we could not determine a regulation of col1α1 mRNA expression in α7KO [44] and therefore involvement of nAChR in collagen synthesis might be tissue specific. nAChR subunit a3 implies a part of the nicotine-collagen pathway in skin [42] whereas nAChR subunit α9 might be responsible for it in bone. Alterations in collagen fiber arrangement, secreted collagen products in blood serum as well as cellular regulation on mRNA and protein level were found in animals of osteoporosis models as well as in samples of patients with osteoporosis [45–47]. Thus, the decrease in Col1α1 mRNA expression in bone of α9KO support our results of |iCT (Tb.Pf, SMI) and biomechanical measurements (bending stiffness, maximal breaking force) regarding the first phases of bone mass reductions by means of structural alterations.

At the mRNA level, we measured a reduction of Cx43 expression in α9KO compared to α9WT. Cx43 is a transmembrane protein which is involved in hexameric hemichannels (connexons) that can be combined with connexons of other cells by formation of gap junctions [48]. Cx43 is the most abundant connexin in bone. It is found in osteoblasts, os- teocytes, and osteoclasts [48]. Using immunohistochemistry we detected Cx43 amongst others in osteoblasts where its involvement in proper fracture healing was reported for cell type specific Cx43 KO mice. Global Cx43 KO mice exhibited a delayed osteoblast differentiation and bone mineralization [49]. However, intensive immuno-positive structures in α9KO, α10KO and WT were found in vessels, osteocytic dendrites and the gap junctions between the osteocytes as shown by a strong macular and thin fibrillary staining around osteocytes. Deletion of osteocytic Cx43 resulted in an enhanced apoptosis of osteocytes, faster aging, reduced cortical area fraction and cortical bone material strength, and increased periosteal bone formation [49]. In analogy with osteocytic Cx43 deletion, we found a reduced strength in cortical bone as measured by biomechanical tests in α9KO. In skin, nAChR α9 is involved in cell-cell as well as cell-matrix adhesion [13]. Blocking of nAChR α9 leads to skin blisters and faulty regulation of keratinocyte adhesion [50]. Thus, it is possible that deletion of nAChR subunit α9 is implicated in defects in cell-cell contacts of osteocytes. Osteocytes have an important role in defect healing as well as remodeling. They

detect the mechanical strain, regulate bone formation via osteoblasts and bone resorption via osteoclasts. One of the most important molecules of osteocytes involved in these processes is sclerostin which is nearly exclusively synthetized by osteocytes and its up- regulation inhibits bone formation [51]. In α9 and α10KO mice, we did not find an altered expression of sclerostin at mRNA or protein level. We observed immunohistochemical labeling for sclerostin in some osteocytes while neighboring osteocytes showed no immunolabeling. This somehow inconsistent staining pattern was also described by Robling et al. and is considered to be normal for osteocytes because mechanical loading is different for every osteocyte even if they are arranged in the same trabeculae [52].

On the ultrastructural level, we observed a reduced number of healthy osteocytes and a higher number of degenerating and dying osteocytes in α9KO compared to α9WT. Dying osteocytes express and secrete factors such as receptor of nuclear factor kappa B ligand (RANKL) which stimulates osteoclastogenesis and leads to chemotactic movement of osteoclasts towards damaged osteocytes where bone matrix will be degraded [51]. Thus, the reduction of Cx43 together with the ultrastructural signs of degeneration in osteocytes might be a significant reason for the biomechanical weakness, the alterations of typical μCT parameters like SMI and Tb.Pf. No significant differences in ultrastructure were found for α10KO compared to α10WT. Therefore, it would be interesting to investigate the bone status of the recently generated double KO mice of α9α10 nAChR [53] and bone cell specific KO mice in an up-coming study. One limitation of our study is the usage of constitutive gene KOs that could have systemic impacts, e.g. input of the nervous system that might interfere with typical effects in bone. It may also be of interest in future studies to perform functional assays for e.g. ALP, TRAP, and collagen of bone and serum.

Recently, the expression of subunits α9 and α10 was reported in several brain regions [10] where they might be involved in the regulation of behavior and activity. Impaired physical activity connected with muscle degeneration and loss of bone mass could explain the alteration of α9KO bone status. To test this, a hang test was performed on α9KO mice, but did not find significant changes compared to the α9WTs. The brain secretome includes several hormones that strongly influence bone homeostasis and osteocyte function. Mohammadi et al. (2017) described a dysregulation of the hypothalamus-pituitary-gland axis by disruption of the circadian rhythm in α9α10KO that altered hormone release [54] and might therefore be involved in pathological alterations of bone.

5. Conclusions

In summary, we reported here the reduced biomechanical strength, decreased cortical TMD and alterations in trabecular microarchitecture in nAChR α9KO mice that mirror the characteristic properties of an osteopenic bone. In addition, we detected reduced expression of Col1α1 and Cx43 as well as a higher number of degenerated and dying osteo- cytes in α9KO compared to α9WT. The nAChR α9 subunit seems to be involved in regulation of matrix formation by osteoblasts and the cellcell contacts of osteocytes. Therefore, lack of activity of nAChRs containing α9 subunits might modify the osteocytic regulation of bone remodeling followed by alterations in bone phenotype that result in the bony characteristics of osteopenia.

Supplementary Material

Refer to Web version on PubMed Central for supplementary material.

Acknowledgments

The authors thank Ivonne Bergen, Olga Dakischew, Gunhild Martels, and Ida Oberst for skillful technical assistance and Dr. Ursula Sommer for TEM analysis. This study was supported by German Research Society (DFG SFB/TRR 79 projects B7, Z3 to VK, KSL and MK as well as KR 4338/1-1 to GKC) and grant support NIH R21DC015124 to DEV. The UMMC Animal Behavior Core is funded through an NIH Institutional Development Award (IDeA) from the National Institute of General Medical Sciences (P30 GM103328). The study is part of the thesis of L. Baumann.

References

[1]. Mandl P, Hayer S, Karonitsch T, Scholze P, Gyori D, Sykoutri D, Bluml S, Mocsai A, Poor G, Huck S, Smolen JS, Redlich K, Nicotinic acetylcholine receptors modulate osteoclastogenesis, Arthritis Res. Ther 18 (2016) 63. [PubMed: 26970742]

[2]. Bajayo A, Bar A, Denes A, Bachar M, Kram V, Attar-Namdar M, Zallone A, Kovacs KJ, Yirmiya R, Bab I, Skeletal parasympathetic innervation communicates central IL-1 signals regulating bone mass accrual, Proc. Natl. Acad. Sci. U. S. A 109 (2012) 15455–15460. [PubMed: 22949675]

[3]. Lips KS, Kneffel M, Willscheid F, Mathies FM, Kampschulte M, Hartmann S, Panzer I, Durselen L, Heiss C, Kauschke V, Altered ultrastructure, density and cathepsin K expression in bone of female muscarinic acetylcholine receptor M3 knockout mice, Int. Immunopharmacol 29 (2015) 201–207. [PubMed: 26002583]

[4]. Kalamida D, Poulas K, Avramopoulou V, Fostieri E, Lagoumintzis G, Lazaridis K, Sideri A, Zouridakis M, Tzartos SJ, Muscle and neuronal nicotinic acetylcholine receptors. Structure, function and pathogenicity, FEBS J. 274 (2007) 3799–3845. [PubMed: 17651090]

[5]. Elgoyhen AB, Vetter DE, Katz E, Rothlin CV, Heinemann SF, Boulter J, α10: a determinant of nicotinic cholinergic receptor function in mammalian vestibular and cochlear mechanosensory hair cells, Proc. Natl. Acad. Sci. U. S. A 98 (2001) 3501–3506. [PubMed: 11248107]

[6]. Sgard F, Charpantier E, Bertrand S, Walker N, Caput D, Graham D, Bertrand D, Besnard F, A novel human nicotinic receptor subunit, α10, that confers functionality to the α9-subunit, Mol. Pharmacol 61 (2002) 150–159. [PubMed: 11752216]

[7]. Romero HK, Christensen SB, Di Cesare Mannelli L, Gajewiak J, Ramachandra R, Elmslie KS, Vetter DE, Ghelardini C, Iadonato SP, Mercado JL, Olivera BM, McIntosh JM, Inhibition of α9α10 nicotinic acetylcholine receptors prevents chemotherapy-induced neuropathic pain, Proc. Natl. Acad. Sci. U. S. A 114 (2017) E1825–E1832. [PubMed: 28223528]

[8]. Peng H, Ferris RL, Matthews T, Hiel H, Lopez-Albaitero A, Lustig LR, Characterization of the human nicotinic acetylcholine receptor subunit alpha (alpha) 9 (CHRNA9) and alpha (alpha) 10 (CHRNA10) in lymphocytes, Life Sci. 76 (2004) 263–280. [PubMed: 15531379]

[9]. Hecker A, Kullmar M, Wilker S, Richter K, Zakrzewicz A, Atanasova S, Mathes V, Timm T, Lerner S, Klein J, Kaufmann A, Bauer S, Padberg W, Kummer W, Janciauskiene S, Fronius M, Schweda EK, Lochnit G, Grau V, Phosphocholine-modified macromolecules and canonical nicotinic agonists inhibit ATP-induced IL-1beta release, J. Immunol 195 (2015) 2325–2334. [PubMed: 26202987]

[10]. Lykhmus O, Voytenko LP, Lips KS, Bergen I, Krasteva-Christ G, Vetter DE, Kummer W, Skok M, Nicotinic acetylcholine receptor α9 and α10 subunits are expressed in the brain of mice, Front. Cell. Neurosci 11 (2017) 282. [PubMed: 28955208]

[11]. Chen CS, Lee CH, Hsieh CD, Ho CT, Pan MH, Huang CS, Tu SH, Wang YJ, Chen LC, Chang YJ, Wei PL, Yang YY, Wu CH, Ho YS, Nicotine-induced human breast cancer cell proliferation attenuated by garcinol through down-regulation of the nicotinic receptor and cyclin D3 proteins, Breast Cancer Res. Treat 125 (2011) 73–87. [PubMed: 20229177]

[12]. Lee CH, Huang CS, Chen CS, Tu SH, Wang YJ, Chang YJ, Tam KW, Wei PL, Cheng TC, Chu JS, Chen LC, Wu CH, Ho YS, Overexpression and activation of the α9-nicotinic receptor

during tumorigenesis in human breast epithelial cells, J. Natl. Cancer Inst 102 (2010) 1322–1335. [PubMed: 20733118]

[13]. Chernyavsky AI, Arredondo J, Vetter DE, Grando SA, Central role of α9 acetylcholine receptor in coordinating keratinocyte adhesion and motility at the initiation of epithelialization, Exp. Cell Res 313 (2007) 3542–3555. [PubMed: 17706194]

[14]. Chikova A, Grando SA, Naturally occurring variants of human A9 nicotinic receptor differentially affect bronchial cell proliferation and transformation, PLoS One 6 (2011) e27978. [PubMed: 22125646]

[15]. Luo L, Bennett T, Jung HH, Ryan AF, Developmental expression of α9 acetylcholine receptor mRNA in the rat cochlea and vestibular inner ear, J. Comp. Neurol. 393 (1998) 320–331. [PubMed: 9548553]

[16]. Zablotni A, Dakischew O, Trinkaus K, Hartmann S, Szalay G, Heiss C, Lips KS, Regulation of acetylcholine receptors during differentiation of bone mesenchymal stem cells harvested from human reaming debris, Int. Immunopharmacol 29 (2015) 119–126. [PubMed: 26215588]

[17]. En-Nosse M, Hartmann S, Trinkaus K, Alt V, Stigler B, Heiss C, Kilian O, Schnettler R, Lips KS, Expression of non-neuronal cholinergic system in osteoblast-like cells and its involvement in osteogenesis, Cell Tissue Res. 338 (2009) 203–215. [PubMed: 19820967]

[18]. Che X, Guo J, Wang L, Miao C, Ge L, Tian Z, Wang J, Involvement of the nonneuronal cholinergic system in bone remodeling in rat midpalatal suture after rapid maxillary expansion, Biomed. Res. Int 2016 (2016) 8106067. [PubMed: 27478838]

[19]. Guo J, Wang L, Xu H, Che X, Expression of non-neuronal cholinergic system in maxilla of rat in vivo, Biol. Res 47 (2014) 72. [PubMed: 25723857]

[20]. Ma Y, Li X, Fu J, Li Y, Gao L, Yang L, Zhang P, Shen J, Wang H, Acetylcholine affects osteocytic MLO-Y4 cells via acetylcholine receptors, Mol. Cell. Endocrinol 384 (2014) 155–164. [PubMed: 24508663]

[21]. Vetter DE, Katz E, Maison SF, Taranda J, Turcan S, Ballestero J, Liberman MC, Elgoyhen AB, Boulter J, The a10 nicotinic acetylcholine receptor subunit is required for normal synaptic function and integrity of the olivocochlear system, Proc. Natl. Acad. Sci. U. S. A 104 (2007) 20594–20599. [PubMed: 18077337]

[22]. Vetter DE, Liberman MC, Mann J, Barhanin J, Boulter J, Brown MC, Saffiote-Kolman J, Heinemann SF, Elgoyhen AB, Role of α9 nicotinic ACh receptor subunits in the development and function of cochlear efferent innervation, Neuron 23 (1999) 93–103. [PubMed: 10402196]

[23]. Rontgen V, Blakytny R, Matthys R, Landauer M, Wehner T, Gockelmann M, Jermendy P, Amling M, Schinke T, Claes L, Ignatius A, Fracture healing in mice under controlled rigid and flexible conditions using an adjustable external fixator, J. Orthop. Res 28 (2010) 1456–1462. [PubMed: 20872581]

[24]. Kauschke V, Kneffel M, Floel W, Hartmann S, Kampschulte M, Durselen L, Ignatius A, Schnettler R, Heiss C, Lips KS, Bone status of acetylcholinesterase- knockout mice, Int. Immunopharmacol 29 (2015) 222–230. [PubMed: 26250336]

[25]. Bouxsein ML, Boyd SK, Christiansen BA, Guldberg RE, Jepsen KJ, Muller R, Guidelines for assessment of bone microstructure in rodents using micro-computed tomography, J. Bone Miner. Res 25 (2010) 1468–1486. [PubMed: 20533309]

[26]. van't Hof RJ, Rose L, Bassonga E, Daroszewska A, Open source software for semi-automated histomorphometry of bone resorption and formation parameters, Bone 99 (2017) 69–79. [PubMed: 28366796]

[27]. Taylor SE, Shah M, Orriss IR, Generation of rodent and human osteoblasts, Bonekey Rep. 3 (2014) 585, 10.1038/bonekey.2014.80. [PubMed: 25396049]

[28]. Orriss IR, Hajjawi MO, Huesa C, MacRae VE, Arnett TR, Optimisation of the differing conditions required for bone formation in vitro by primary osteoblasts from mice and rats, Int. J. Mol. Med 34 (2014) 1201–1208, 10.3892/ijmm.2014.1926 . [PubMed: 25200658]

[29]. Cowin SC, Cardoso L, Blood and interstitial flow in the hierarchical pore space architecture of bone tissue, J. Biomech 48 (2015) 842–854. [PubMed: 25666410]

[30]. Enlow DH, Functions of the Haversian system, Am. J. Anat 110 (1962) 269–305. [PubMed: 13890323]

[31]. Cardoso L, Fritton SP, Gailani G, Benalla M, Cowin SC, Advances in assessment of bone porosity, permeability and interstitial fluid flow, J. Biomech 46 (2013) 253–265. [PubMed: 23174418]

[32]. Lips KS, Bruggmann D, Pfeil U, Vollerthun R, Grando SA, Kummer W, Nicotinic acetylcholine receptors in rat and human placenta, Placenta 26 (2005) 735–746. [PubMed: 16226123]

[33]. Bruggmann D, Lips KS, Pfeil U, Haberberger RV, Kummer W, Multiple nicotinic acetylcholine receptor alpha-subunits are expressed in the arterial system of the rat, Histochem. Cell Biol 118 (2002) 441–447. [PubMed: 12483309]

[34]. Toda N, Toda H, Nitric oxide-mediated blood flow regulation as affected by smoking and nicotine, Eur. J. Pharmacol 649 (2010) 1–13. [PubMed: 20868673]

[35]. Feitelson JB, Rowell PP, Roberts CS, Fleming JT, Two week nicotine treatment selectively increases bone vascular constriction in response to norepinephrine, J. Orthop. Res 21 (2003) 497–502. [PubMed: 12706023]

[36]. McIntosh JM, Absalom N, Chebib M, Elgoyhen AB, Vincler M, α9 nicotinic acetylcholine receptors and the treatment of pain, Biochem. Pharmacol 78 (2009) 693–702. [PubMed: 19477168]

[37]. Hahn M, Vogel M, Pompesius-Kempa M, Delling G, Trabecular bone pattern factor—a new parameter for simple quantification of bone microarchitecture, Bone 13 (1992) 327–330. [PubMed: 1389573]

[38]. Hildebrand T, Ruegsegger P, Quantification of bone microarchitecture with the structure model index, Comput. Methods Biomech. Biomed. Engin 1 (1997) 15–23. [PubMed: 11264794]

[39]. Chen H, Kubo KY, Segmental variations in trabecular bone density and microstructure of the spine in senescence-accelerated mouse (SAMP6): a murine model for senile osteoporosis, Exp. Gerontol 47 (2012) 317–322. [PubMed: 22342532]

[40]. Salmon PL, Ohlsson C, Shefelbine SJ, Doube M, Structure model index does not measure rods and plates in trabecular bone, Front. Endocrinol 6 (2015) 162 Lausanne.

[41]. Eltony SA, Ali SS, Histological study on the effect of nicotine on adult male guinea pig thin skin, Anat. Cell Biol 50 (2017) 187–199. [PubMed: 29043097]

[42]. Arredondo J, Hall LL, Ndoye A, Nguyen VT, Chernyavsky AI, Bercovich D, Orr-Urtreger A, Beaudet AL, Grando SA, Central role of fibroblast a3 nicotinic acetylcholine receptor in mediating cutaneous effects of nicotine, Lab. Investig 83 (2003) 207–225. [PubMed: 12594236]

[43]. Sekhon HS, Keller JA, Proskocil BJ, Martin EL, Spindel ER, Maternal nicotine exposure upregulates collagen gene expression in fetal monkey lung. Association with a7 nicotinic acetylcholine receptors, Am. J. Respir. Cell Mol. Biol 26 (2002) 31–41. [PubMed: 11751201]

[44]. Vicary GW, Ritzenthaler JD, Panchabhai TS, Torres-Gonzalez E, Roman J, Nicotine stimulates collagen type I expression in lung via a7 nicotinic acetylcholine receptors, Respir. Res 18 (2017) 115. [PubMed: 28576119]

[45]. Viguet-Carrin S, Garnero P, Delmas PD, The role of collagen in bone strength, Osteoporos. Int 17 (2006) 319–336. [PubMed: 16341622]

[46]. Silva MJ, Brodt MD, Wopenka B, Thomopoulos S, Williams D, Wassen MH, Ko M, Kusano N, Bank RA, Decreased collagen organization and content are associated with reduced strength of demineralized and intact bone in the SAMP6 mouse, J. Bone Miner. Res 21 (2006) 78–88. [PubMed: 16355276]

[47]. Daghma DES, Malhan D, Simon P, Stotzel S, Kern S, Hassan F, Lips KS, Heiss C, El Khassawna T, Computational segmentation of collagen fibers in bone matrix indicates bone quality in ovariectomized rat spine, J. Bone Miner. Metab 36 (3) (2017) 297–306. [PubMed: 28589410]

[48]. Plotkin LI, Davis HM, Cisterna BA, Saez JC, Connexins and pannexins in bone and skeletal muscle, Curr. Osteoporos. Rep 15 (2017) 326–334. [PubMed: 28647887]

[49]. Plotkin LI, Stains JP, Connexins and pannexins in the skeleton: gap junctions, hemichannels and more, Cell. Mol. Life Sci 72 (2015) 2853–2867. [PubMed: 26091748]

[50]. Nguyen VT, Ndoye A, Grando SA, Novel human α9 acetylcholine receptor regulating keratinocyte adhesion is targeted by Pemphigus vulgaris autoimmunity, Am. J. Pathol 157 (2000) 1377–1391. [PubMed: 11021840]

[51]. Chen H, Senda T, Kubo KY, The osteocyte plays multiple roles in bone remodeling and mineral homeostasis, Med. Mol. Morphol 48 (2015) 61–68. [PubMed: 25791218]

[52]. Robling AG, Niziolek PJ, Baldridge LA, Condon KW, Allen MR, Alam I, Mantila SM, Gluhak-Heinrich J, Bellido TM, Harris SE, Turner CH, Mechanical stimulation of bone in vivo reduces osteocyte expression of Sost/sclerostin, J. Biol. Chem 283 (2008) 5866–5875. [PubMed: 18089564]

[53]. Morley BJ, Dolan DF, Ohlemiller KK, Simmons DD, Generation and characterization of α9 and α10 nicotinic acetylcholine receptor subunit knockout mice on a C57BL/6J background, Front. Neurosci 11 (2017) 516. [PubMed: 28983232]

[54]. Mohammadi SA, Burton TJ, Christie MJ, α9-nAChR knockout mice exhibit dysregulation of stress responses, affect and reward-related behaviour, Behav. Brain Res 328 (2017) 105–114. [PubMed: 28408300]

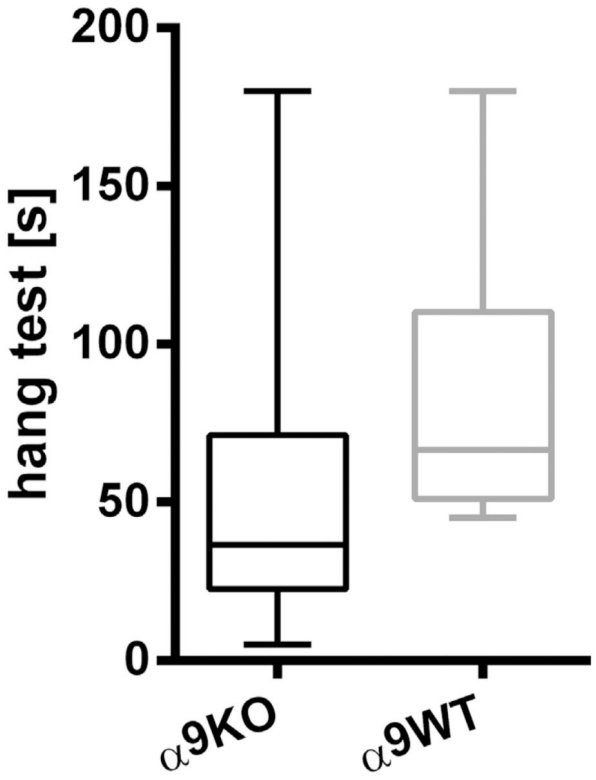

Fig. 1.

Mouse hang test. Measurement of hanging time of α9KO and α9WT in seconds (s). α9KO: knockout mice of nicotinic acetylcholine receptor subunit α9; α9WT: corresponding wild type mice of α9KO.

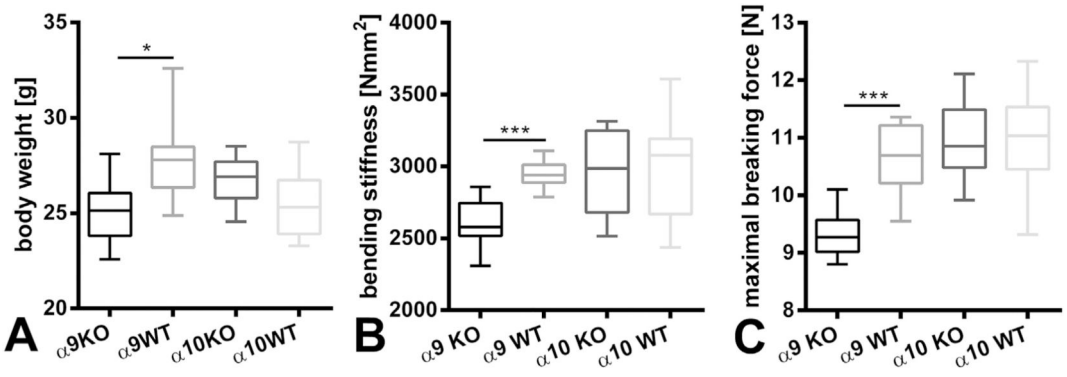

Fig. 2.

Bone strength. Measurement of (A) body weight, (B) bending stiffness, (C) maximal breaking force of knockout mice of the α9 and α10 subunits of nicotinic acetylcholine receptors (α9KO, α10KO) and their corresponding wild type mice (WT). * $p \leq 0.05$; *** $p \leq 0.001$.

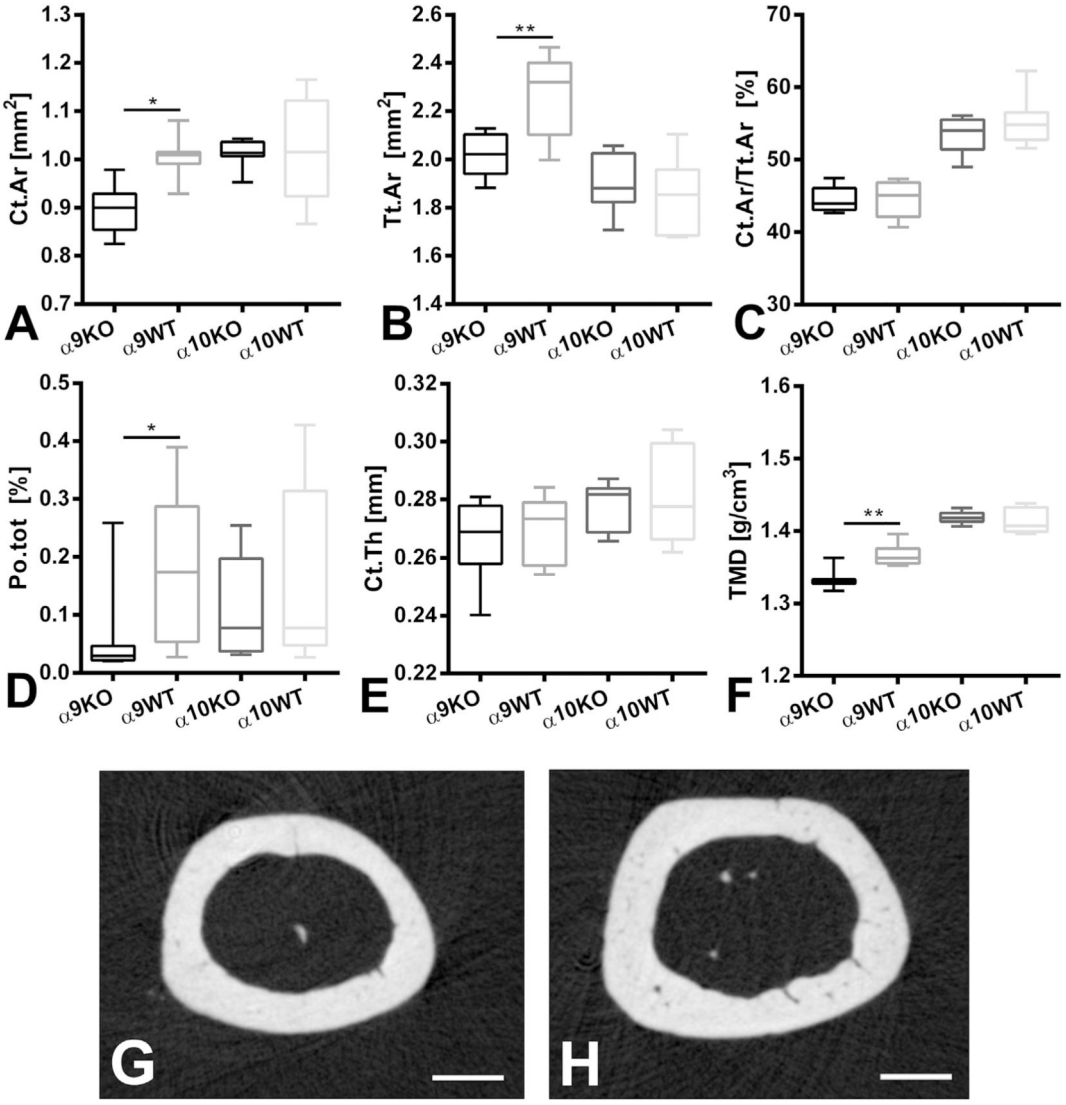

Fig. 3.

Microarchitecture of mid diaphyseal femur cortex. Calculation of (A) cortical bone area (Ct.Ar), (B) total cross-sectional area inside the periosteal envelope (Tt.Ar), (C) cortical area fraction (Ct.Ar/Tt.Ar), (D) total porosity (Po.tot), (E) 3-dimensional cortical thickness (Ct.Th 3D), (F) tissue mineral density (TMD), and 2D picture of μCT scan of (G) knockout mice of nicotinic acetylcholine receptor subunit α9 (α9KO) and (H) the corresponding wild type mice (α9WT). α10KO: knockout mice of nicotinic acetylcholine receptor subunit α10; α10WT: corresponding wild type mice of α10KO. * $p \leq 0.05$; ** $p \leq 0.01$. Scale bar: 400 μm.

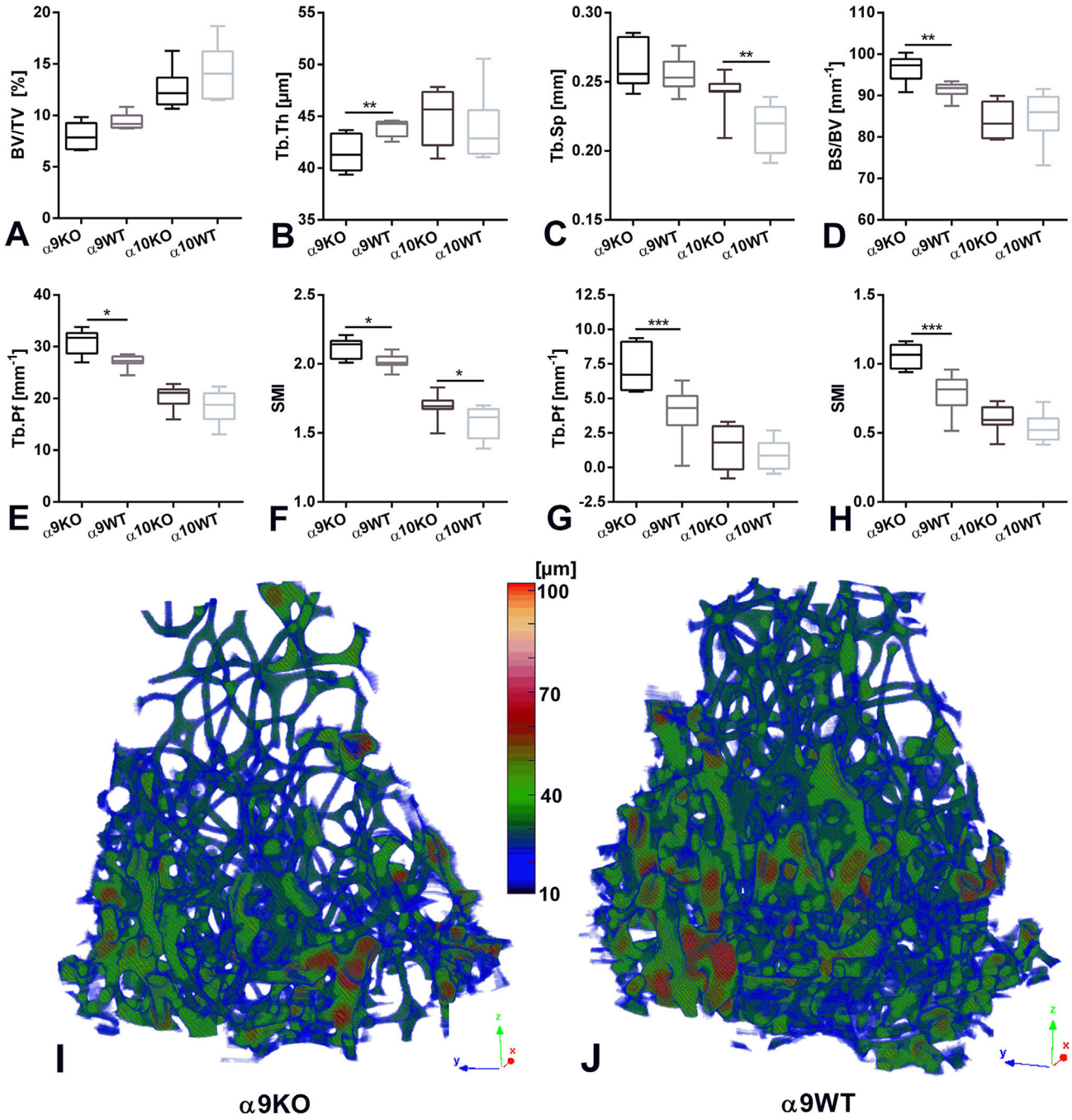

Fig. 4.

Microarchitecture of trabecular bone. Determination of (A) bone volume fraction (BV/TV), (B) trabecular thickness (Tb.Th), (C) trabecular separation (Tb.Sp), (D) specific bone surface (BS/BV), (E) trabecular pattern factor (Tb.Pf), (F) structure model index (SMI) of right distal femur and (G) Tb.Pf, (H) SMI of vertebrae L1, (I) 3D-color coded model of trabecular thickness of α9KO and (J) α9WT distal femur metaphysis. α9KO: knockout mice of nicotinic acetylcholine receptor subunit α9; α10KO: knockout mice of nicotinic acetylcholine receptor subunit α10; α9WT: corresponding wild type mice of α9KO;

α10WT: corresponding wild type mice of α10KO. * $p \leq 0.05$; ** $p \leq 0.01$; *** $p \leq 0.001$. (For interpretation of the references to color in this figure legend, the reader is referred to the web version of this article.)

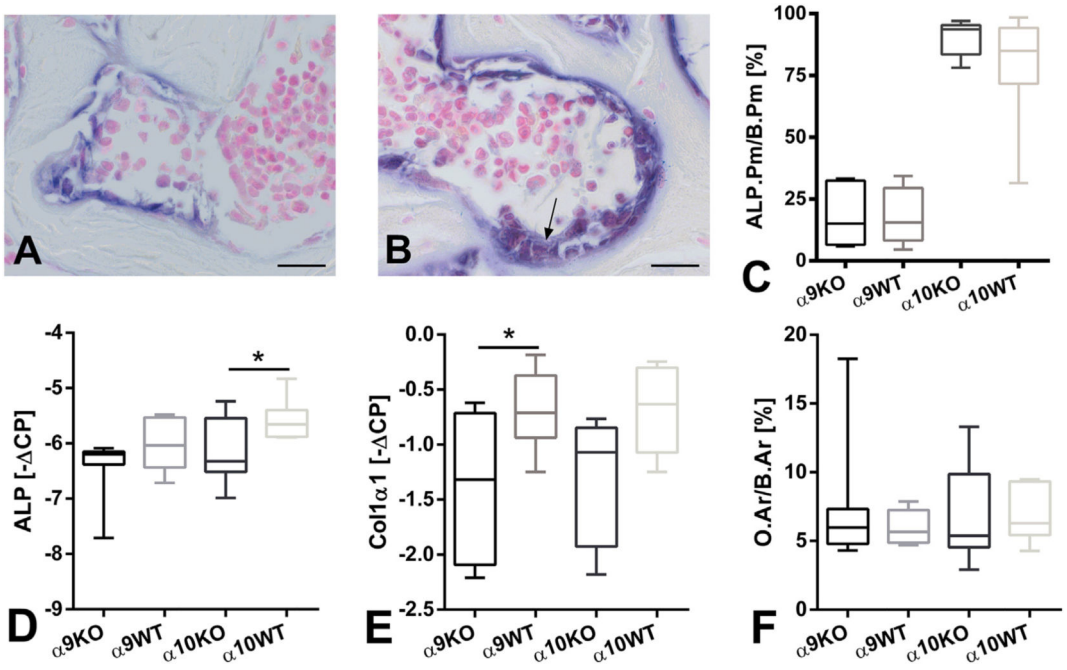

Fig. 5.

Osteoblasts. Alkaline phosphatase (ALP) enzyme histochemical staining of (A) α9WT and (B) α10KO. Arrow in B marks single ALP positive osteoblasts. Scale bar: 20 μm. (C) Histomorphometrical calculation of relative ALP perimeter (ALP.Pm/B.Pm) using the ALP enzyme histochemical stainings. mRNA expression analysis of (D) ALP and (E) collagen 1α1 (Col1α1) by means of real-time RT-PCR. Measurement of relative osteoid area (O.Ar/B.Ar) by means of histomorphometrical analysis of Kossa-van-Gieson staining. α9KO: knockout mice of nicotinic acetylcholine receptor subunit α9; α10KO: knockout mice of nicotinic acetylcholine receptor subunit α10; α9WT: corresponding wild type mice of α9KO; α10WT: corresponding wild type mice of α10KO. * $p \leq 0.05$.

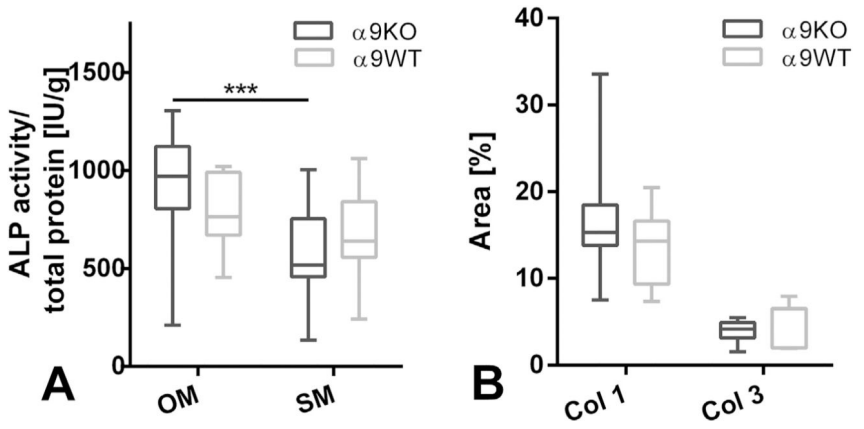

Fig. 6.

Cell culture experiments of neonatal osteoblasts. (A) ALP activity per total protein of α9KO and α9WT cultured in osteogenic differentiation medium (OM) and standard medium (SM). (B) Histomorphometrical analysis of Picro- Sirius-Red positive stained area of α9KO and α9WT osteoblasts in osteogenic differentiation medium. α9KO: knockout mice of nicotinic acetylcholine receptor subunit α9; α9WT: corresponding wild type mice of α9KO. Col 1: collagen type 1, Col 3: collagen type 3. *** $p \leq 0.001$.

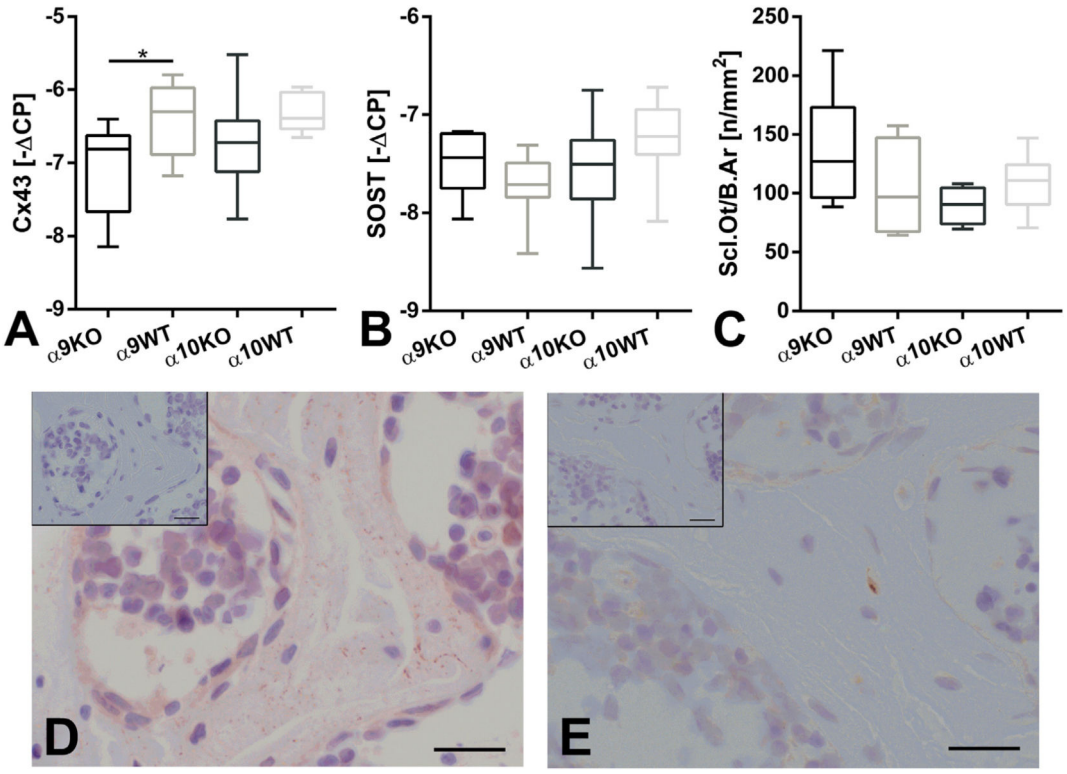

Fig. 7.

Osteocytes. Determination of mRNA expression of (A) connexin 43 (Cx43), (B) *SOST,* and (C) histomorphometrical quantification of slcerostin im- munopositive osteocytes per bone area (Scl.Ot/B.Ar). Immunohistochemical labeling of osteocytes and their dendrites with (D) antiserum against Cx43 (exemplary picture of α9KO) and (E) sclerostin (exemplarily for α10WT). α9KO: knockout mice of nicotinic acetylcholine receptor subunit α9; α10KO: knockout mice of nicotinic acetylcholine receptor subunit α10; α9WT: corresponding wild type mice of α9KO; α10WT: corresponding wild type mice of α10KO. * $p \leq 0.05$. Scale bar: 20 μm.

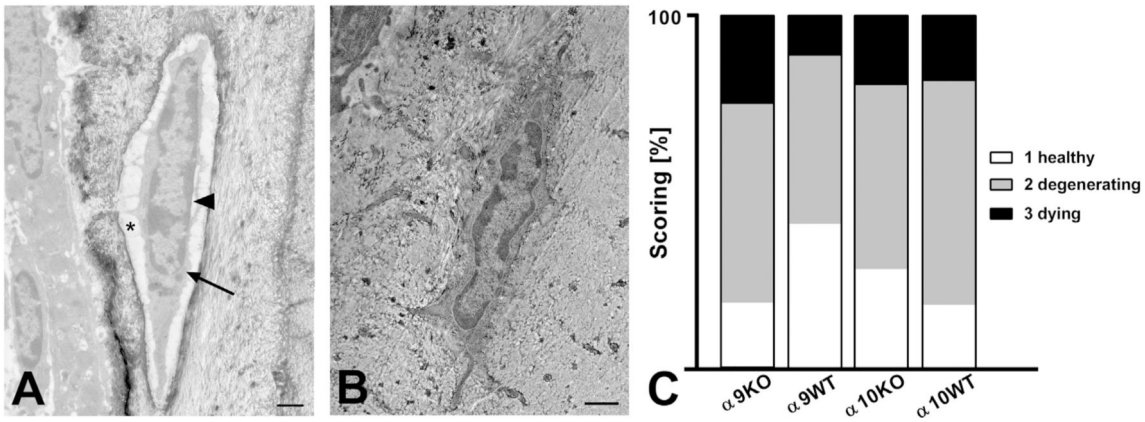

Fig. 8.

Transmission electron microscopy (TEM) of osteocytes. (A) Osteocyte of α9KO with enlarged pericellular space (star), folding of the cytoplasm membrane (arrow), and enlarged space between the two membranes of nucleus (arrow head). (B) Healthy osteocyte of α9WT. (C) Scoring results with significantly increased number of degenerated and dying osteocytes in α9KO compared to α9WT while no significant difference was measured for α10KO and WT. Score 1: healthy, score 2: degenerating, score 3: dying osteocytes. Scale bar: 2 μm.

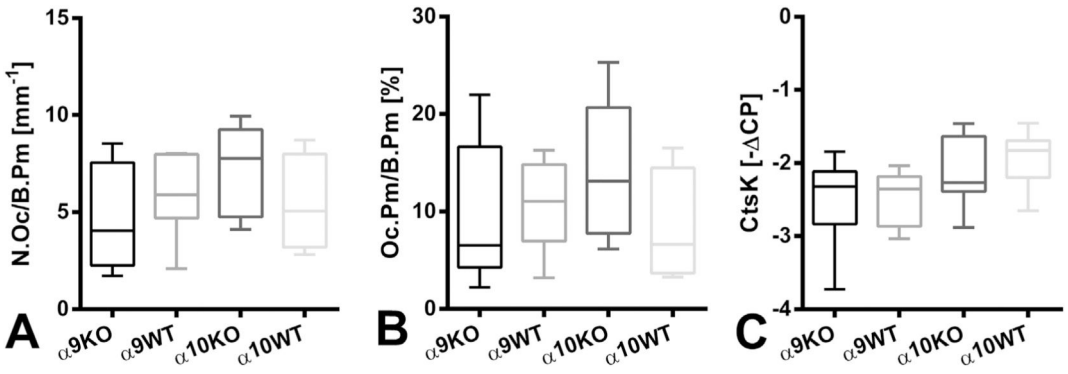

Fig. 9.

Osteoclasts. Histomorphomectical calculation of TRAP stainings of (A) number of osteoclasts per bone perimeter (N.Oc/B.Pm), (B) relative osteoclast perimeter (Oc.Pm/B.Pm) and (C) mRNA expression of Cathepsin K (CtsK) by means of real-time RT-PCR. α9KO: knockout mice of nicotinic acetylcholine receptor subunit α9; α10KO: knockout mice of nicotinic acetylcholine receptor subunit α10; α9WT: corresponding wild type mice of α9KO; α10WT: corresponding wild type mice of α10KO.

Table 1

Primer pairs used for real-time RT-PCR.

Primer		Sequence	Length [bp[h]]	GenBank ID (accession)
ALP[a]	for[b]	TCAGCTAATGCACAATATCAAGG	87	NM_007431.2
	rev[c]	TCCACATCAGTTCTGTTCTTCG		
Col 1α1[d]	for	TGGCATCCCTGGACAGCCTG	144	NM_007742.3
	rev	ATGGGGCCAGGCACGGAAAC		
CtsK[e]	for	GAGGCGGCTATATGACCACT	119	NM_007802.3
	rev	CTTTGCCGTGGCGTTATACA		
Cx43[f]	for	TGCTTCCTCTCACGTCCCAC	127	NM_010288.3
	rev	CGCGATCCTTAACGCCCTTG		
SOST[g]	for	GCCTCCTCCTGAGAACAACC	143	NM_024449.6
	rev	GGCATGGGCCGTCTGTC		
βactin	for	TGTTACCAACTGGGACGACA	165	NM_007393.3
	rev	GGGGTGTTGAAGGTCTCAAA		

[a]ALP: alkaline phosphatase.

[b]for: forward.

[c]rev: reverse.

[d]Col1α1: Collagen 1α1.

[e]CtsK: Cathepsin K.

[f]Cx43: Connexin 43.

[g]SOST: sclerostin.

[h]bp: base pairs.